Insights into the mechanical properties of several triply periodic minimal surface lattice structures made by polymer additive manufacturing

I. Maskery [a], [*], L. Sturm [b], A.O. Aremu [a], A. Panesar [a], [1], C.B. Williams [b], C.J. Tuck [a], R.D. Wildman [a], I.A. Ashcroft [a], R.J.M. Hague [a]

[a] *Centre for Additive Manufacturing, Faculty of Engineering, University of Nottingham, Nottingham NG7 2RD, UK*
[b] *Virginia Polytechnic Institute and State University, Blacksburg, VA 24061, USA*

ABSTRACT

Three-dimensional lattices have applications across a range of fields including structural lightweighting, impact absorption and biomedicine. In this work, lattices based on triply periodic minimal surfaces were produced by polymer additive manufacturing and examined with a combination of experimental and computational methods. This investigation elucidates their deformation mechanisms and provides numerical parameters crucial in establishing relationships between their geometries and mechanical performance. Three types of lattice were examined, with one, known as the primitive lattice, being found to have a relative elastic modulus over twice as large as those of the other two. The deformation process of the primitive lattice was also considerably different from those of the other two, exhibiting strut stretching and buckling, while the gyroid and diamond lattices deformed in a bending dominated manner. Finite element predictions of the stress distributions in the lattices under compressive loading agreed with experimental observations. These results can be used to create better informed lattice designs for a range of mechanical and biomedical applications.

© 2017 The Authors. Published by Elsevier Ltd. This is an open access article under the CC BY license (http://creativecommons.org/licenses/by/4.0/).

1. Introduction

Cellular solids, which include foams, honeycombs and regularly repeating lattice structures, have for some time been investigated due to their various useful properties [1,2]. Chief among these is their inherently lightweight nature, but also of interest is their ability to absorb compressive energy effectively [3–7], act as heat exchangers [8–10] and provide acoustic [11] and vibrational damping [12]. These properties, combined with the emerging capabilities of additive manufacturing (AM) to fabricate complex lattice structures, make cellular solids attractive for advanced mechanical applications; in the transport sector for example, where the performance of lightweight components may be enhanced by exploiting several of these features in highly optimised designs.

A notable recent application has seen biocompatible AM cellular

solids used in orthopaedic implants, where their controllable porosity and stiffness enable them to act as scaffolds for bone and tissue integration, helping to reduce the problem of stress shielding associated with solid implants [13–17]. The range of available AM processes means these cellular structures can be made in a broad spectrum of materials, from gels and polymers to high strength metal alloys.

A key challenge facing the designer of a lattice structure for a specific application is that of choosing appropriate lattice design variables. The lattice material, cell type and volume fraction play crucial roles in determining the structural stiffness and strength, but the exact relationships between these properties are generally poorly understood for all but the simplest type of lattice. The same is true of thermal, electrical and acoustic properties. This is especially problematic for any attempt at combining lattice structures with topology optimisation (TO), a common tool for the design of materially-efficient AM components [18–20]. Thus, it is crucial that robust relationships between cell geometry and performance are established.

In this paper we investigate three lattice structures based on

---

triply periodic minimal surfaces (TPMS). The lattice types are the gyroid, diamond and primitive, and they are examined with a combination of mechanical testing and finite element analysis (FEA). We examine the behaviour of these lattice types under compressive loading, and compare their respective stress-strain curves, elastic moduli, collapse strengths, deformation processes and numerically determined stress distributions. We also provide a set of numerical parameters which can be used in models linking geometry and mechanical performance for these lattice types.

TPMS lattices were chosen for this study because they offer several potential advantages over the strut-based lattices (body-centred-cubic, for example) more commonly manufactured and investigated using AM. The properties of TPMS lattice structures include a good combination of specific stiffness and axisymmetric stiffness [21], high surface-to-volume ratio [22] and pore connectivity, reduced need for surface skinning [23], ease of functional grading [24—27], choice of network and matrix phases with non-connected voids [22] and variable conductivity through choice of cell type [28]. Owing to these properties TPMS lattices have found applications in biomedicine [15—17], as well as photovoltaic [29] and electrochromic devices [30]. A range of TPMS lattice types, including those examined here, were recently fabricated in a biocompatible rubber-like material and characterised by Blanquer et al. [31], who determined their respective surface curvatures, pore sizes and water permeabilities.

Following this introduction we outline our methodology for TPMS lattice structure design, manufacture and investigation. This includes the provision of lattice design relationships allowing the volume fraction of several TPMS cell types to be specified via their governing spatial equations. In section 4 we present and discuss the results of our experimental and numerical investigations. This is the first instance of gyroid, diamond and primitive AM lattice structures having been experimentally examined together in a single investigation. Our conclusions are provided in section 5.

2. Theoretical background

For mechanical applications, the most straightforward method of choosing the appropriate lattice volume fraction, or relative density, for a given loading scenario is to use the semi-empirical formulae of Gibson, Ashby et al. [1]. For cellular solids made from materials that have a plastic yield point, Gibson and Ashby introduced the equations

$$\frac{E_{latt.}}{E_{sol.}} = C_1 \left(\frac{\rho_{latt.}}{\rho_{sol.}} \right)^n, \tag{1a}$$

$$\frac{\sigma_{pl.\ latt.}}{\sigma_{y\ sol.}} = C_5 \left(\frac{\rho_{latt.}}{\rho_{sol.}} \right)^m, \tag{1b}$$

where the relevant physical properties are given in Table 1.

For the prefactors C_1 and C_5, which 'include all of the geometric constants of proportionality' [1], Gibson, Ashby et al. provide a range of values from 0.1—4.0 and 0.1—1.0, respectively, while n and m are ~ 2 and $\sim \frac{3}{2}$, respectively, when deformation occurs by bending of the cellular struts or walls [1,2]. These values come from a survey of existing metal foam data, with each parameter depending on the geometry and, in particular, the deformation mechanisms of the cells in question. The elastic modulus and plateau stress of equivalently dense lattice structures may therefore vary greatly if they comprise cells of different geometries, with Deshpande et al. [32] and Zheng et al. [33] having shown that n and m may be much closer to unity for cellular structures which deform through stretching rather than bending.

To use equations (1a) and (1b) for effective lattice structure design, either by manually selecting an appropriate volume fraction or through implementation of a combined lattice-TO approach, one must know the Gibson-Ashby prefactors, C_1 and C_5, and exponents, n and m, for the chosen lattice cell type. There currently exists only limited data regarding these variables for lattice structures made by AM. They may be determined experimentally, by manufacturing and testing lattice specimens of varying volume fraction, then applying appropriate fitting to the mechanical data. Such an approach was taken by Yan et al. [34,35] and Dalaq et al. [36], who examined AM metal and polymer lattices, respectively. Other methods include finite element calculations, as were also used by Dalaq et al. [36,37], and the construction of analytical models based on structural failure mechanisms, as was done by Usijima et al. [38] and Khaderi et al. [39].

The theoretical study by Kapfer et al. [40] is especially interesting, as they assessed the potential for a numerical quantifier arising from the cell geometry to differentiate the mechanical performance of different lattice types. Using results from finite element calculations, they found a correlation between values of $X_{perc.}$, a parameter computed from the cell geometry, and the relative bulk moduli of the cells. The findings of Kapfer et al. [40] indicate a complementary and potentially useful method for predicting the mechanical performance of lattice structures; a method that is not reliant upon mechanical testing or extensive finite element calculations, but does capture the influence of cell geometry.

3. Methodology

3.1. Design and fabrication of the TPMS lattice structures

Gyroid (G), diamond (D) and primitive (P) lattice structures with arbitrary numbers of cells and volume fractions can be generated by finding the $U = 0$ isosurface of the TPMS equations [41,42],

$$\begin{aligned} U_G = {}& \cos(k_x x)\sin(k_y y) + \\ & \cos(k_y y)\sin(k_z z) + \\ & \cos(k_z z)\sin(k_x x) - t, \end{aligned} \tag{2a}$$

$$\begin{aligned} U_D = {}& \sin(k_x x)\sin(k_y y)\sin(k_z z) + \\ & \sin(k_x x)\cos(k_y y)\cos(k_z z) + \\ & \cos(k_x x)\sin(k_y y)\cos(k_z z) + \\ & \cos(k_x x)\cos(k_y y)\sin(k_z z) - t, \end{aligned} \tag{2b}$$

$$U_P = \cos(k_x x) + \cos(k_y y) + \cos(k_z z) - t, \tag{2c}$$

and treating this surface as the boundary between solid and void material phases. For each of the above, k_i are the TPMS function periodicities, defined by

$$k_i = 2\pi \frac{n_i}{L_i} \quad (\text{with } i = x, y, z), \tag{3}$$

where n_i are the numbers of cell repetitions in the directions x, y and z, and L_i are the absolute sizes of the structure in those directions.

In equations (2a)—(2c), t can be used as a variable to control the volume fraction, ρ^*, of the resulting lattice structure. The relationship between t and ρ^* is unique for each TPMS cell type; relationships for the gyroid, diamond and primitive cell types were determined for this work and are provided in Fig. 1, where inset images show the effect of varying t on the thickness of the cell members in a gyroid lattice structure.

The general methodology for using TPMS equations to produce

Table 1
Physical and mechanical properties for the description of lattices under compression.

Notation	Physical or mechanical property
$\rho_{latt.}$	Density of the lattice structure
$\rho_{sol.}$	Density of the material constituting the lattice struts or walls
ρ^*	Relative density, or volume fraction, of the lattice; equal to $\rho_{latt.}/\rho_{sol.}$
$\varepsilon_{latt.}$	Effective strain of the lattice structure
$E_{latt.}$	Elastic modulus of the lattice structure
$E_{sol.}$	Elastic modulus of the material constituting the lattice struts or walls
E^*	Relative elastic modulus of the lattice; equal to $E_{latt.}/E_{sol.}$
$\sigma_{latt.}$	Effective stress of the lattice structure
$\sigma_{pl.\ latt.}$	Compressive strength of the lattice structure
$\sigma_{y\ sol.}$	Yield strength of the material constituting the lattice struts or walls
σ^*	Relative collapse strength of the lattice; equal to $\sigma_{pl.\ latt.}/\sigma_{y\ sol.}$

files for manufacture and FE analysis is presented in Fig. 2. The 3D field representing U is created first, being based on the designer's choice of volume fraction and cell repetitions in each direction. A triangular mesh may then be determined at the $U = 0$ boundary and exported as an STL file or similar boundary representation. For FE analysis, regions of space where $U \leq 0$ are defined to be solid and regions where $U > 0$ are defined to be void. From this definition, a hexahedral FE mesh describing the lattice structure can trivially be obtained.

Prior to choosing a lattice configuration for fabrication and experimental testing, a preliminary FE investigation was performed in which diamond lattice configurations from $1 \times 1 \times 1$ to $5 \times 5 \times 5$ tessellating cells were examined. Each structure had a volume fraction of 0.3 and a cell size of 10 mm. They were designed using software developed at the University of Nottingham (which is available upon request from the corresponding author). The elastic modulus of the diamond lattice structure increased with the number of unit cells, asymptotically approaching an upper bound; for the case of the diamond structure presented in Fig. 3, this was determined using an exponential fit to be 102 MPa.

The incrementally increasing elastic modulus can be attributed to the diminishing effect of cells with free surfaces on the overall stiffness of the lattice structure. As boundary conditions were imposed only on the top and bottom surfaces of the structures, the four vertical planes defining the edges of the cubic structures were free to deform. With increasing cell repetitions in the lattice, a level of homogeneity in the deformation is introduced as the previously free planes at the cell edges are constrained by the adjoining cells, giving a more accurate description of the cell deformation as if it were part of a homogeneous porous solid. The asymptote modulus of 102 MPa could therefore be used in a continuum model to represent this lattice type and loading direction. This would be especially beneficial if it was situated inside a large, complex component, for example, where simulating the whole lattice would incur prohibitively high computational demands. It is interesting to note that using the modulus obtained from FE of a single unit cell in such a continuum model would result in an underestimation of the stiffness by around 20%.

In Fig. 3 the $4 \times 4 \times 4$ lattice arrangement provided an elastic modulus just 0.2% below the upper bound, thus providing a good estimate of the lattice structure's elastic modulus, with significantly reduced computational expense thanks to the smaller number of elements than would be required to model a lattice with $5 \times 5 \times 5$ cells or more.

With these results in mind, for the main part of this investigation, a series of gyroid, diamond and primitive lattice structures with dimensions $40 \times 40 \times 40$ mm and volume fraction 0.3 were designed. The cell size was $10 \times 10 \times 10$ mm, meaning each

structure contained a $4 \times 4 \times 4$ arrangement of TPMS cells. CAD representations of the unit cells and lattice structures are shown in Fig. 4.

Three specimens of each lattice type were manufactured by selective laser sintering (SLS) from EOS polyamide PA2200, which is based on nylon 12. The manufacturing platform was an EOS P100 machine, and the SLS processing parameters are given in Table 2. The d10, d50 and d90 sizes of the powder particles based on the particle size distribution were 35 μm, 54 μm and 82 μm, respectively. Photographs of the manufactured lattices samples are shown in Fig. 5. The masses and dimensions of all the lattice samples were recorded after manufacture; their volume fractions were very consistent, providing a mean of $\rho^* = 0.294 \pm 0.007$, which agrees within experimental uncertainty with the designed volume fraction of 0.3.

3.2. Mechanical testing

Following the methodology used in a previous examination of SLS lattice structures [4], the lattice specimens were mechanically compressed using an Instron 5966 universal testing machine equipped with a 50 kN load cell. The deformation rate was 0.25 mm/s, and a video camera was used to record the lattices during the tests. Individual frames were extracted from the videos and are presented in section 4 to illustrate the mechanisms of progressive collapse in the structures.

The elastic modulus and yield strength of SLS PA 2200 were determined from stress-strain curves of solid coupons tested under tension and compression - see Fig. 6. Like the lattice specimens, they were tested using an Instron 5966 universal testing machine with a 50 kN load cell. In each case three specimens were examined and the yield strength was determined at 0.2% offset strain.

For the tensile behaviour we tested standard dog bone coupons (ISO 527) manufactured with their long axes parallel to the SLS build plane; the results were $E_{sol.} = 1.80 \pm 0.05$ GPa and $\sigma_{y\ sol.} = 29.1 \pm 0.8$ MPa. For the compressive behaviour we tested cubes of size $(20\ \text{mm})^3$; the results were $E_{sol.} = 1.59 \pm 0.02$ GPa and $\sigma_{y\ sol.} = 44.5 \pm 0.3$ MPa. The material's modulus under compression
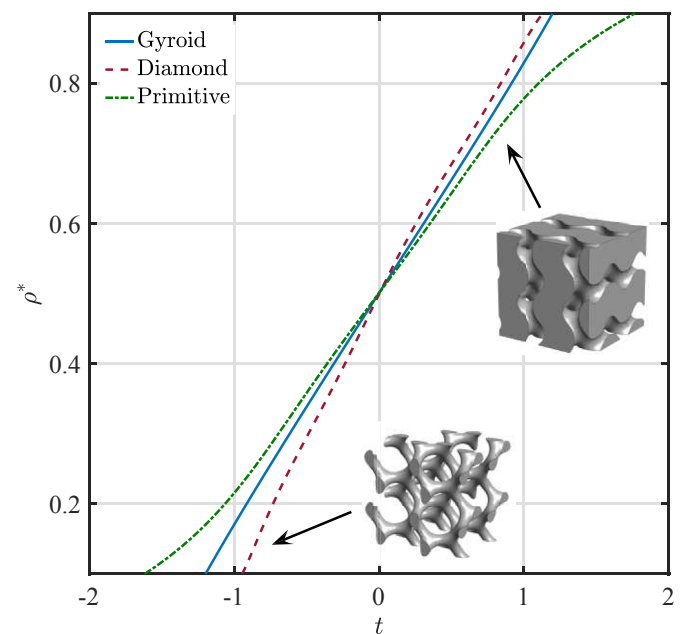
Fig. 1. Relationships between the TPMS equation parameter t and relative density, ρ^*, of corresponding lattice cells.
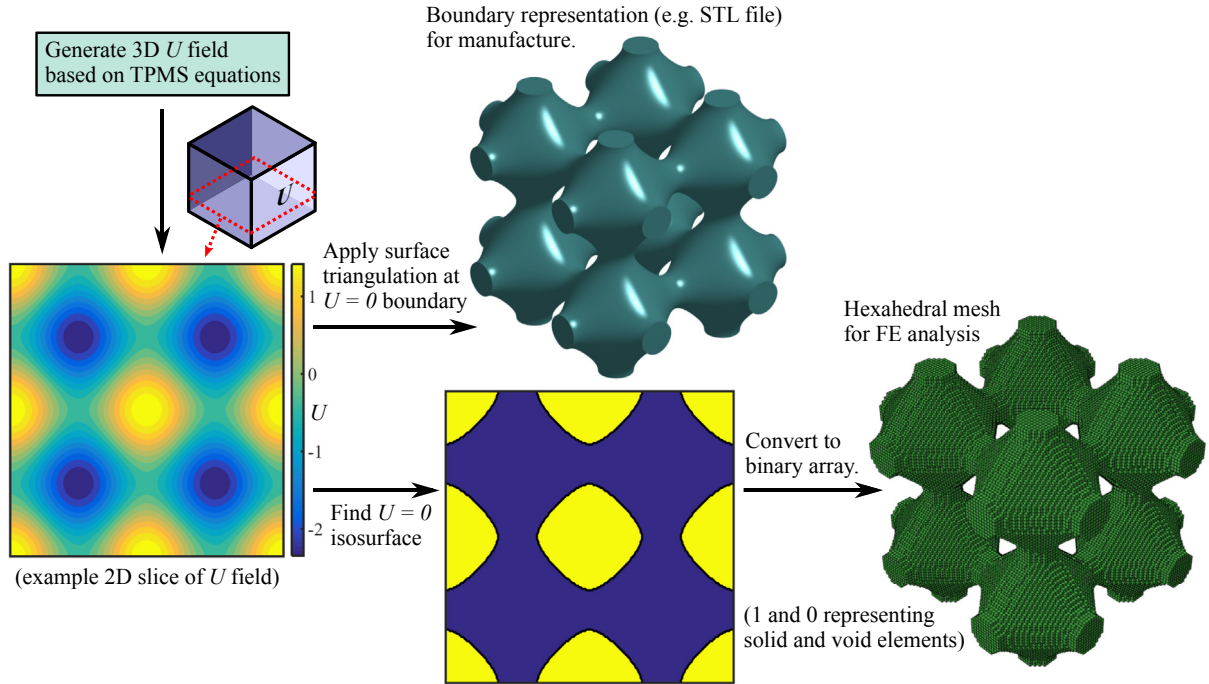
Fig. 2. General method for creating boundary representations (e.g. the STL file format commonly used in additive manufacturing) and hexahedral meshes for FE analysis based on TPMS equations. This particular example shows the creation of a primitive lattice with a 2 × 2 × 2 array of cells and volume fraction of 0.3.
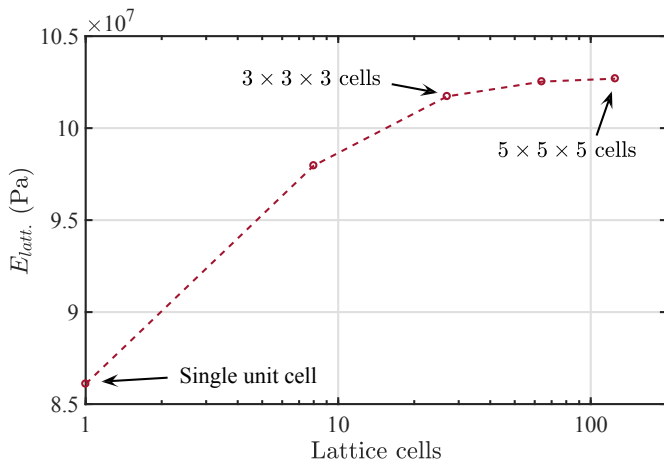
Fig. 3. Evolution of elastic modulus with increasing number of unit cells in the diamond lattice structure.

is lower than it is under tension, a finding previously reported for SLS nylon 12 by Ngim et al. [43]. Our data indicates that the compressive modulus is 88% of the tensile modulus, whereas Ngim et al. [43] put the value at 46%.

3.3. Finite element analysis

Gyroid, diamond and primitive lattice structures were explicitly modelled with hexahedral finite element meshes using the Abaqus/Standard 2016 FEA solver (Dassault Systemes - Vélizy-Villacoublay, France). All elements were linear, reduced-integration solid elements; type *C3D8R*, following the Abaqus labelling scheme. The lattice models were subjected to compressive displacements of 0.4 mm (equivalent to 1% strain) at all of the nodes of their top planes, as illustrated in Fig. 7. Rotation of the bottom plane nodes

was allowed only around the *z* axis, while translation was allowed only in the *xy* plane (the *ZSYMM* boundary condition as implemented in Abaqus). The same boundary condition applied to the nodes of the top plane. The elements were assigned elastic moduli corresponding to those determined by testing solid SLS PA 2200 coupons - more details are provided in section 4.2.

As illustrated in Fig. 2, finite element models were constructed by mapping binary voxel representations of the lattices directly into hexahedral meshes. This approach allowed the aspect ratio each element to be fixed at 1, thus avoiding FEA errors associated with distorted elements that can arise during meshing operations. Discretisation errors were minimised by increasing the number of elements in the FEA calculations and observing the resulting change in elastic modulus. The mesh size for each structure was progressively increased until elastic modulus convergence was reached, with the elastic modulus being simply found from

$$E_{latt. \text{ (FEA)}} = \frac{FL}{Au}, \tag{4}$$

where *F* is the total reaction force at the top surface of the structure, *L* is original height of the lattice (40 mm), *A* is the cross-sectional area of the lattice domain (1600 mm²) and *u* is the displacement of the top surface in the loading direction (0.4 mm).

Fig. 8 shows the effect of mesh size on the elastic moduli of the examined lattices. FE convergence was defined as occurring when the change in elastic modulus between subsequent calculations with different mesh sizes fell below 1% - see the inset to Fig. 8. For the gyroid and diamond structures this was achieved with around three million elements in the model, which is equivalent to an element size of (186 μm)³. For the primitive structure only two million elements were required, equivalent to an element size of (213 μm)³. These element sizes were used to obtain the main FE results provided in section 4.2.
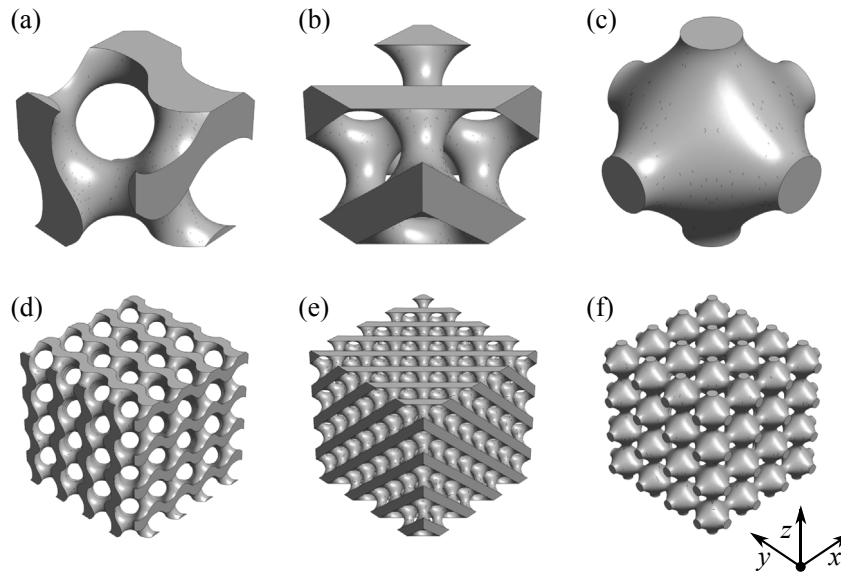
Fig. 4. Individual gyroid, diamond and primitive cells with $\rho^* = 0.3$ are shown in (a), (b) and (c), respectively, while lattice structures comprising $4 \times 4 \times 4$ cells are shown in (d), (e) and (f).

Table 2
SLS parameters used in the production of the TPMS lattice structures for mechanical testing.

SLS parameter	
Laser power	21 W
Laser scan speed	2500 mm/s
Laser hatch spacing	250 μm
Powder bed temperature	173 °C
Powder deposition thickness	100 μm
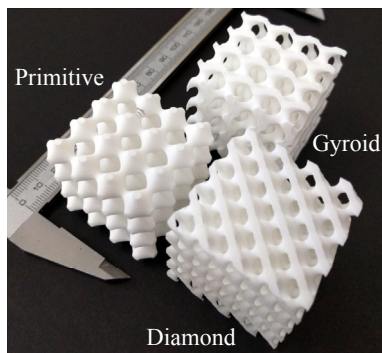
Fig. 5. Gyroid, diamond and primitive lattice structures, as manufactured by SLS.

Fig. 6. Tensile and compressive stress-strain curves for solid SLS PA 2200.

4. Results and discussion

4.1. Compressive deformation behaviour

Before the lattice stress-strain data are presented, some additional nomenclature must be established. Fig. 9 includes $\varepsilon_{latt.}$ as an axis label. This is the effective total strain experienced by the lattice structure, as if it were a uniform $40 \times 40 \times 40$ mm specimen of arbitrary homogeneous material. This should not be confused with the localised strains in the cellular struts. Similarly, $\sigma_{latt.}$ is the effective stress of the whole structure, found by dividing the applied load by the specimen area of 1600 mm², and does not refer to local stresses in the struts. Cellular solids have been analysed in

this manner since the work of Gibson, Ashby et al. [1], allowing straightforward identification of the key features of cellular solid deformation.

Representative stress-strain curves from compressive testing of the gyroid, diamond and primitive lattices are presented in Fig. 9. The gyroid and diamond structures showed stress-strain behaviour quite similar to one another, and also characteristic of compressive deformation in plastically yielding open cellular solids; that is, they exhibited initial regions of linear elasticity followed by long plastic plateaux. The elastic moduli extracted from the linear elastic regions for all three lattice types are given in Table 3, from which it can be seen that those of the gyroid and diamond lattices agreed within experimental uncertainty.

The stress-strain curve of the primitive lattice structure is substantially different from those of the other two. It has a gradient change at around 3% strain, marking the termination of linear elastic behaviour. The elastic modulus extracted from this region is 192±1 MPa, which is over 100% greater than those of the gyroid and diamond lattices.
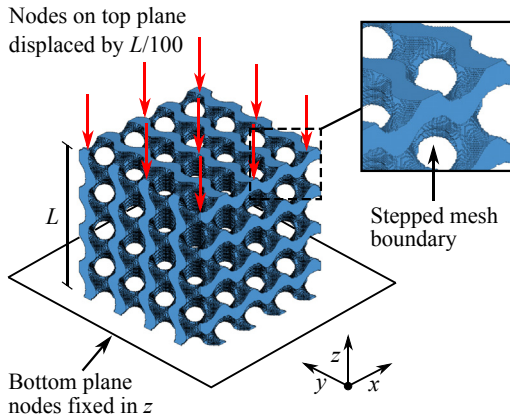
Fig. 7. A representative hexahedral mesh used for TPMS lattice structure FEA calculations.

The principal differentiating feature in the stress-strain curves of the three TPMS lattice types is the post-yield behaviour. The plastic plateaux of the gyroid and diamond lattices are typical of cellular solids, in particular those whose deformation is bending dominated, but the primitive lattice, unusually, shows increasing strength up to a peak at 14% strain, closely followed by structural weakening and collapse. This behaviour indicates that the deformation of the primitive lattice, loaded in the z direction as here, may be stretching dominated; a result which is congruent with it having a much higher elastic modulus than the other two lattice types [32,33,44].

The inset plots of Fig. 9, which are the gradients $d\sigma/d\varepsilon$ for the gyroid and primitive lattices, suggest that in the post-yield $3 - 14\%$ strain region the primitive lattice undergoes a combination of elastic and plastic deformation. This hypothesis is supported in part by a geometric evaluation of the lattice, particularly the variation of

its load-bearing cross-section, as presented in Fig. 10. The relative cross-sectional area of the primitive cell varies from a minimum of 0.05 at the cell edges to a maximum of 0.63 toward the centre, naturally leading to the formation of thin 'neck' regions of the lattice. These will generally have higher stresses under axial loading, and are therefore likely to enter plasticity prior to other regions.

The relative load-bearing cross-sections of the gyroid and diamond cells vary by around ± 0.03 and ± 0.04, respectively, from their mean values of 0.3, and this variation occurs more frequently over the cell height, leading to a more uniform distribution of material throughout the structure. The deformation of the primitive lattice in the region $3 - 14\%$ strain can therefore be seen as being due to local plastic deformation in the thin neck regions accompanied by persisting elasticity in the thicker central nodes.

The nature of the primitive lattice's weakening and collapse at 14% strain, and the reason for its large elastic modulus compared to those of the other structures, is elucidated by the video recordings of their respective compression tests. Fig. 11 shows video frames from the compression tests of the three lattice types. Tracking the relative positions of points on the camera-facing surfaces of the samples reveals that deformation in the primitive lattice occurs almost exclusively in the direction of loading at strains less than 14%. The deformation is therefore stretching dominated. Over 14% strain, structural buckling is observed, followed by fracture of the thin neck regions.

In contrast, video frame analysis indicates that the gyroid and diamond lattices undergo bending dominated deformation, which is in keeping with their stress-strain curves. The conclusion that primitive lattices are stretching dominated, while gyroid and diamond lattices are bending dominated is in agreement with the previous classifications of Afshar et al. [27], and Khaderi et al. [39].

After removal of the applied load at 50% deformation, the gyroid and diamond lattice structures, shown in Fig. 12(a) and (b), exhibited some residual elasticity as they expanded in height to
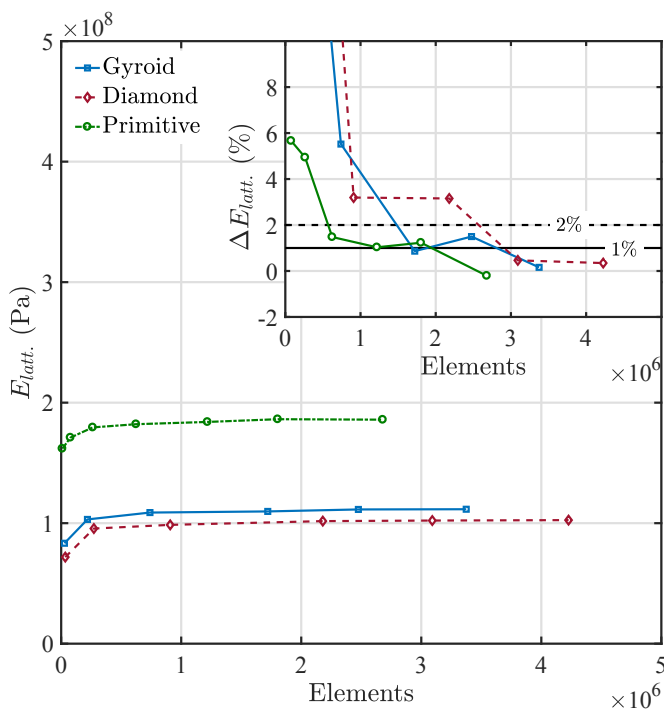

Fig. 8. Evolution of elastic modulus with increasing numbers of elements. Inset: percentage changes in elastic modulus between calculations with increasing mesh sizes.
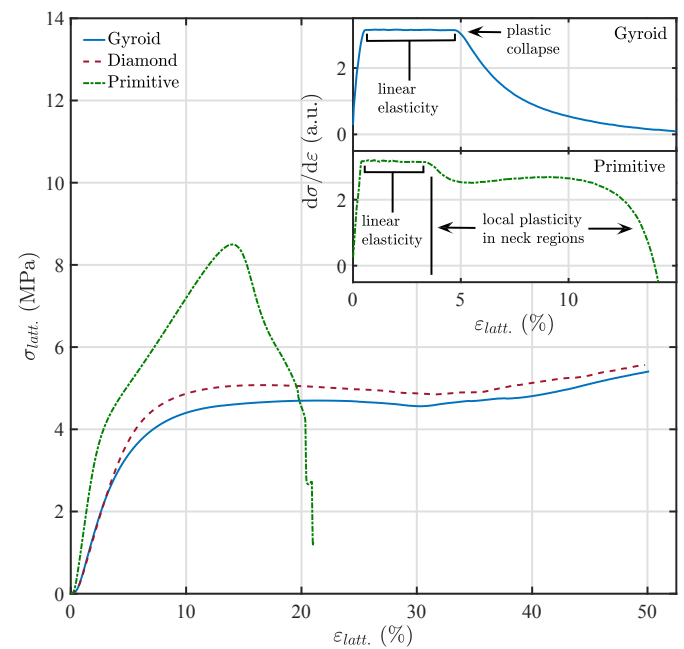

Fig. 9. Compressive stress-strain curves of the gyroid, diamond and primitive lattices. Inset: the gradients $d\sigma/d\varepsilon$ for gyroid and primitive lattices. Note that the increasing gradient of the inset plots below 0.5% strain is due full contact being made with the specimens during compressive testing; it is not a pertinent feature of structural deformation.

Table 3
Elastic moduli and plastic collapse strengths of gyroid, diamond and primitive lattice structures with volume fraction 0.3. Both are given in absolute terms and values relative to the properties of solid SLS PA 2200 material. C_1 and C_5 are determined from equations (1a) and (1b). Gyroid and diamond lattices are treated as being bending dominated, so n and m in equations (1a) and (1b) are given the values 2 and $\frac{3}{2}$, respectively, while for the primitive lattice, which observations suggest is stretching dominated, n and m take the value 1.

	Gyroid	Diamond	Primitive
$E_{latt.}$ (MPa)	95±1	93±1	192±1
E^* ($\times10^{-3}$)	60±1	59±1	121±1
C_1	0.69±0.01	0.68±0.01	0.411±0.005
$\sigma_{pl. latt.}$ (MPa)	3.33±0.08	3.85±0.08	4.11±0.04
σ^* ($\times10^{-3}$)	75±2	86±1	92±1
C_5	0.47±0.01	0.54±0.01	0.313±0.004

30 mm and 31.5 mm, respectively; corresponding to 75% and ~79% of their original heights. The primitive lattices had buckled and fractured in the region 15−20% strain, so were reduced to fragments, as shown in Fig. 12(c). The inset magnified views in Fig. 12(c) show fractures of the vertically and horizontally oriented neck regions. During the failure of the primitive structures, fractures occurred first in the vertically oriented necks, with planes of lattice cells then slipping horizontally (in the xy plane) prior to total structural collapse.

4.2. Finite element analysis

Based on our observations of the deformation processes in the experimentally tested lattice specimens, we chose to assign their elements different elastic moduli during FE simulations. For the gyroid and diamond lattices, which showed evidence of bending during compressive deformation, we used an element modulus of 1.695 GPa, which is the average of the tensile and compressive moduli of solid SLS EOS PA2200. This was done to better reflect the combination of tensile and compressive stresses generated by bending. For the primitive lattice, which appears to deform principally by axial stretching when loaded in the z direction, we used
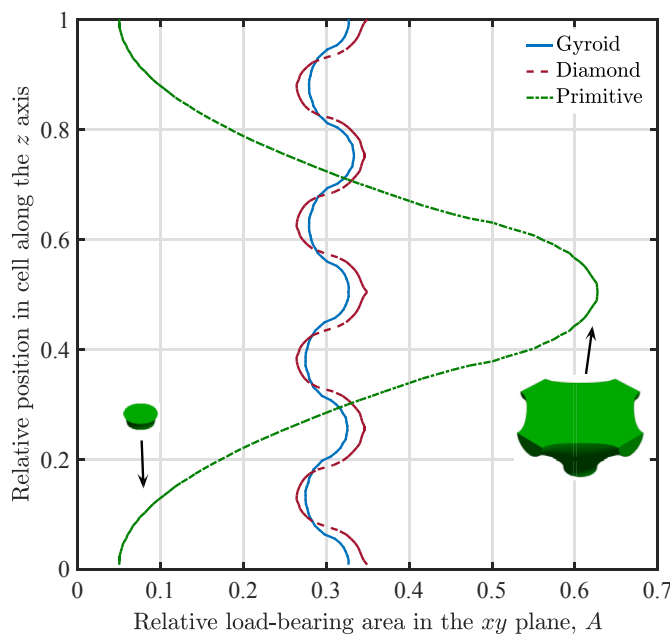
Fig. 10. Relative cross-sectional area of gyroid, diamond and primitive cells along a principal direction x, y, or z.

1.59 GPa, which is purely the compressive modulus of solid SLS EOS PA2200. The predicted elastic moduli of the gyroid, diamond and primitive lattice structures loaded in the z direction are given in Table 4. These were obtained following the FE method laid out in section 3.3.

Von Mises element stresses are shown for the gyroid, diamond and primitive lattices in Fig. 13. The most relevant feature, with respect to the deformation processes discussed above, is that for the primitive lattice the stress is largely localised at the thin neck regions which connect the cell nodes. This supports the idea that these neck regions enter plasticity first under loading along the primitive lattice's columnar directions. The gyroid and diamond lattices exhibit more uniform stress distributions, leading to their deformation behaviour, as evidenced by their stress-strain curves, more closely resembling those of conventional cellular solids such as stochastic foams.

From comparison with Table 3 it can be seen that the order of stiffness, with primitive being the stiffest and diamond the most compliant, is correctly predicted by the FE models, although there is some difference in the actual values. The FE elastic moduli of the gyroid, diamond and primitive lattices differ by 18%, 10% and −4%, respectively, from those obtained from the fabricated specimens. We attribute the overestimation of the gyroid and diamond stiffness to two main factors. First, the lattice moduli resulting from FE simulations are heavily influenced by the choice of modulus assigned to the solid elements. For the gyroid and diamond lattice types, we used an average of tensile and compressive moduli determined from solid SLS EOS PA2200 specimens. Choosing solely the compressive modulus, or an average weighted more towards the compressive modulus, would improve the agreement of the FE moduli with experimental results. For example, assigning the elements of the gyroid and diamond FE models the compressive modulus of solid SLS EOS PA2200 yields lattice moduli which are only 10% and 4% greater than the experimental values from the fabricated specimens.

A second factor we believe to be important is surface roughness. Roughness can lead to reduced stiffness, especially in structures comprising relatively thin members, because it contributes surplus, non load-bearing material at the surface. Profilometry carried out on the solid tensile test coupons revealed an R_z parameter of around 50 μm. The gyroid and diamond lattice structures examined in this work contain members of continuously varying cross-sectional dimensions, with the range 2−3 mm providing a reasonable approximation for both structures. Approximating the worst case, surface roughness could contribute an average of 50 μm of surplus material to these lattice members, reducing their effective load-bearing areas by between 3% and 5%. Under compressive testing, this would result in the fabricated specimens potentially having between 3% and 5% lower stiffness than predicted by FE simulations.

With these factors in mind, it is clear that our FE models do not at present completely capture the deformation mechanics of the experimentally assessed lattices. Whilst incorporation of these factors could increase agreement with experimental values, it is proposed that the current FE models provide sufficient accuracy to enable valid comparison of the different deformation modes and stress distributions in the various lattice types.

4.3. Comparison with previous results

The investigations of Afshar et al. [27], Yan et al. [34] and Khaderi et al. [39] provide the main sources of comparison for the TPMS lattice properties determined here. Table 5 presents the mechanical properties from those authors' works and those from mechanical testing in this study.
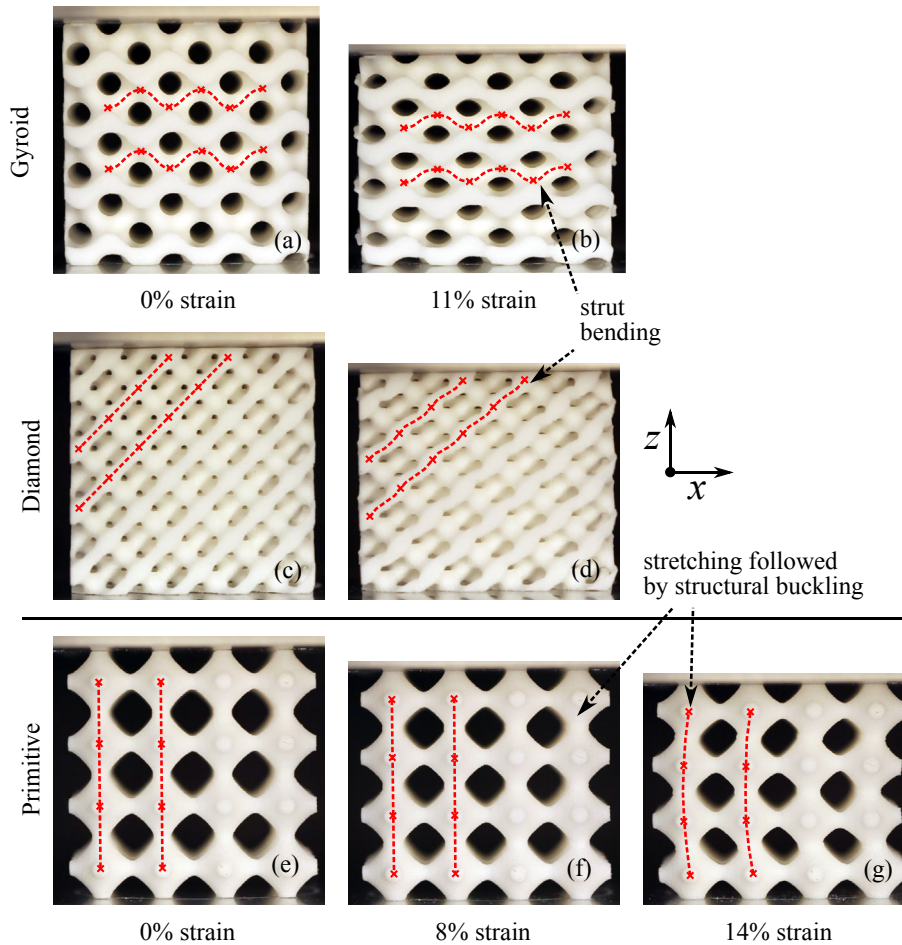
Fig. 11. Video frames showing the deformation of gyroid ((a) and (b)), diamond ((c) and (d)) and primitive ((e), (f) and (g)) lattice structures at a series of compressive strains.

Afshar et al. [27] examined diamond and primitive lattice structures made by polymer jetting. Their specimens had volume fractions of 0.3, the same as those studied here. They observed significant differences in the elastic moduli and yield strengths of the diamond and primitive lattices, ascribing these to their differing deformation mechanisms; the primitive structure being stretching dominated and the diamond structure being bending dominated. This interpretation is supported by the video frame analysis presented here. Afshar et al. [27] also reported the primitive lattice to have an elastic modulus 1.94 times that of the diamond lattice, which is close to the ratio of 2.06±0.01 seen here. Our relative elastic moduli for the diamond and primitive lattices fall inside the range provided by Afshar et al., while the relative collapse strengths we recorded were significantly greater than theirs.

Yan et al. [34] observed that metal gyroid and diamond lattice structures had relative elastic moduli very similar to one another. This is consistent with the evidence presented here; the elastic moduli of the gyroid and diamond lattice structures agree within experimental error. However, our results exceed the predicted values from Yan et al.'s fitting by more than 100%.

Finally, Khaderi et al. [39] examined the gyroid lattice with a combination of FEA and analytical modelling, the latter based on possible collapse modes under uniaxial loading. They showed the gyroid cell to be a bending dominated structure; its elastic modulus and yield strength being dependent on ρ^{*2} and $\rho^{*3/2}$, respectively. The relative elastic modulus obtained here for the gyroid lattice is ∼

57% larger than that predicted by Khaderi et al.'s density-modulus relationship.

In each of these cases, comparisons are made with reports based on lattices of different materials or lower volume fractions than those examined here. It is therefore not surprising that large variations in mechanical properties should arise from these investigations, since the deformation mechanisms of the structures in question will be heavily influenced by the properties of the materials comprising their struts.

5. Conclusions

We have examined three TPMS lattice structures with mechanical compression testing and FE modelling. The cell geometry was seen to play a large role in determining the lattice deformation process and failure mode, as well as the associated stress-strain curve and mechanical properties.

We found that the elastic moduli of TPMS lattices of equivalent volume fraction varied by over 100% depending on the cell geometry, with the primitive lattice type outperforming both the gyroid and diamond. The relatively large elastic modulus of the primitive lattice was obtained at the expense of highly localised plastic deformation, structural buckling and low failure strain. This type of failure is a consequence of the primitive structure's large variation in load-bearing area and associated regions of high stress. Thus, on
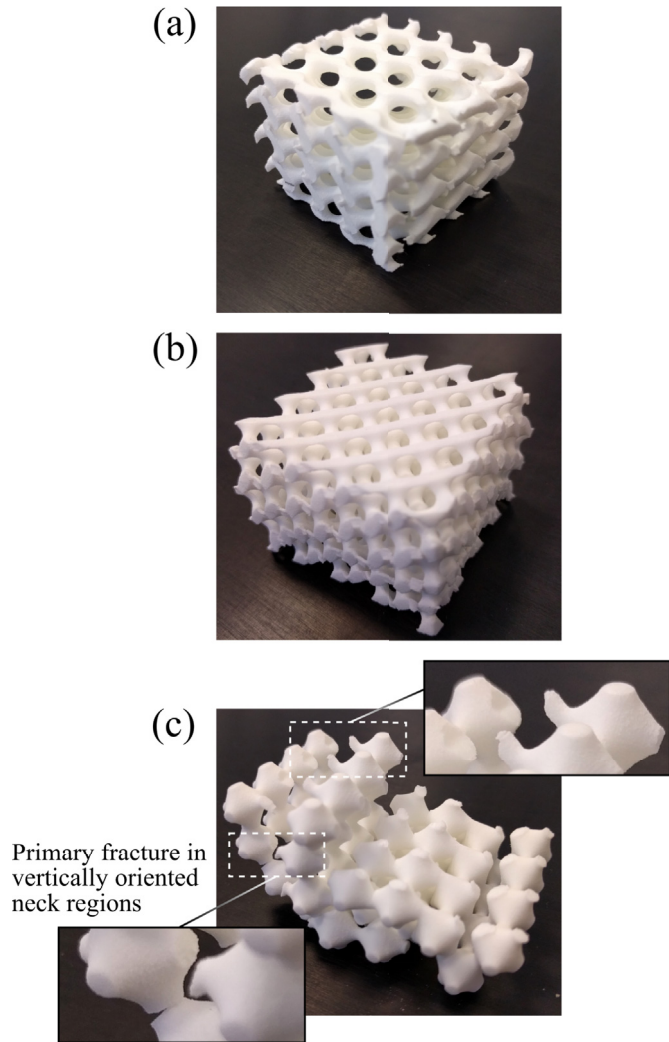
Fig. 12. Photographs showing the gyroid (a), diamond (b) and primitive (c) lattices after compressive testing. The inset in (c) shows fracture close to the thin 'neck' region in the primitive lattice.
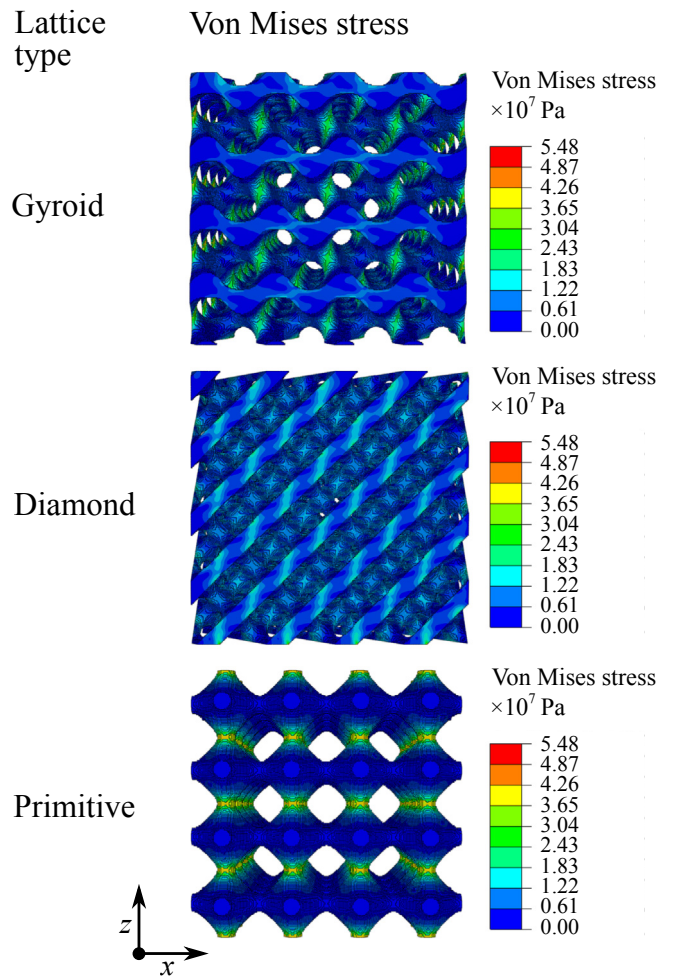

Fig. 13. Von Mises stress distributions in FE compression simulations of gyroid, diamond and primitive lattices.

Table 4
Elastic moduli of gyroid and primitive lattice structures with volume fraction 0.3 obtained from FEA.

	Gyroid	Diamond	Primitive
$E_{latt.\ (FEA)}$ (MPa)	112	102	185

Table 5
Relative elastic moduli, E^*, and collapse strengths, σ^*, of the gyroid (G), diamond (D) and primitive (P) lattices with a volume fraction of 0.3 according to this work and other references. Notes: m - examined metal lattices, p - examined polymer lattices, a - analytical model, f - finite element model, $*$ - volume fraction 0.3, † - extrapolated from volume fractions lower than 0.3.

	E^* ($\times 10^{-3}$)			σ^* ($\times 10^{-3}$)		
	G	D	P	G	D	P
This work	60±1	59±1	121±1	75±2	86±1	92±1
Ref. [27][p,*]	.	42.5 – 94.6	82.6 – 184	.	52.6	46.6
Ref. [34][m,†]	24.2	23.6	.	145	133	.
Ref. [39][a,f,†]	38.3	.	.	72.0	.	.

the basis of this work, we can recommend that a primitive lattice be used in applications requiring high stiffness and strength in one well-defined loading direction. If, on the other hand, the application requires that the latticed part undergoes high strain before failure, a gyroid or diamond lattice would be preferable.

In the context of a previous result which found similar direction-averaged Young's moduli for the TPMS lattice types examined here [40], our findings, which are based on uniaxial loading, suggest a high degree of anisotropy to their mechanical properties. Further investigations in this area will provide more information regarding the direction-specific mechanical performance of these lattices, adding to the currently small set of design rules for optimal lattice structure design.

Another important outcome of this investigation is the determination of relative elastic moduli, relative collapse strengths, and Gibson-Ashby prefactors for three TPMS lattice types. These can now be used in the design of TPMS structures to meet the loading requirements of mechanical and biomedical applications. They will also play a role in establishing the general relationships between lattice properties - material, volume fraction and cell type - and performance that are required for effective AM component design in the future.

In conclusion, our results indicate that informed cell geometry selection can be useful in designing lattice structures to avoid undesirable failure modes, or to provide long plastic plateaux for energy absorption under deformation, therefore reducing the need for extensive FE simulation and mechanical testing.

Acknowledgments

References

[1] L. Gibson, M. Ashby, Cellular Solids: Structure and Properties, Cambridge University Press, 1997.

[2] M. Ashby, A. Evans, N. Fleck, L. Gibson, J. Hutchinson, H. Wadley, Metal Foams: a Design Guide, Butterwoth-Heinemann, 2000.

[3] P.R. Stupak, J.A. Donovan, Deformation and energy absorption of polymer foams as a function of 2-D indenter and absorber geometries, Polym. Eng. Sci. 34 (10) (1994) 857—864.

[4] I. Maskery, A. Hussey, A. Panesar, A. Aremu, C. Tuck, I. Ashcroft, R. Hague, An investigation into reinforced and functionally graded lattice structures, J. Cell. Plast. 53 (2) (2016) 151—165.

[5] I. Maskery, N. Aboulkhair, A. Aremu, C. Tuck, I. Ashcroft, Compressive failure modes and energy absorption in additively manufactured double gyroid lattices, Addit. Manuf. 16 (2017) 24—29.

[6] M. Avalle, G. Belingardi, R. Montanini, Characterization of polymeric structural foams under compressive impact loading by means of energy-absorption diagram, Int. J. Impact Eng. 25 (5) (2001) 455—472.

[7] J. Brennan-Craddock, D. Brackett, R. Wildman, R. Hague, The design of impact absorbing structures for additive manufacture, J. Phys. Conf. Series 382 (1) (2012) 012042.

[8] H. Wadley, D. Queheillalt, Thermal applications of cellular lattice structures, Mater. Sci. Forum 539—543 (2007) 242—247.

[9] J. Tian, T. Lu, H. Hodson, D. Queheillalt, H. Wadley, Cross flow heat exchange of textile cellular metal core sandwich panels, Int. J. Heat Mass Tran. 50 (1314) (2007) 2521—2536.

[10] T. Lu, H. Stone, M. Ashby, Heat transfer in open-cell metal foams, Acta Mater. 46 (11) (1998) 3619—3635.

[11] X. Wang, T.J. Lu, Optimized acoustic properties of cellular solids, J. Acoust. Soc. Am. 106 (2) (1999) 756—765.

[12] P. Göransson, Acoustic and vibrational damping in porous solids, Philos. T. Roy. Soc. A 364 (1838) (2006) 89—108.

[13] L. Murr, S. Gaytan, E. Martinez, F. Medina, R. Wicker, Next generation orthopaedic implants by additive manufacturing using electron beam melting, Int. J. Biomat. 2012 (2012) 245727—245741.

[14] C. Emmelmann, P. Scheinemann, M. Munsch, V. Seyda, Laser additive manufacturing of modified implant surfaces with osseointegrative characteristics, Phys. Procedia 12 (2011) 375—384.

[15] S. Rajagopalan, R.A. Robb, Schwarz meets Schwann: design and fabrication of biomorphic and durataxic tissue engineering scaffolds, Med. Image Anal. 10 (5) (2006) 693—712.

[16] F.P. Melchels, K. Bertoldi, R. Gabbrielli, A.H. Velders, J. Feijen, D.W. Grijpma, Mathematically defined tissue engineering scaffold architectures prepared by stereolithography, Biomaterials 31 (27) (2010) 6909—6916.

[17] F.P. Melchels, A.M. Barradas, C.A. van Blitterswijk, J. de Boer, J. Feijen, D.W. Grijpma, Effects of the architecture of tissue engineering scaffolds on cell seeding and culturing, Acta Biomater. 6 (11) (2010) 4208—4217.

[18] A. Evans, J. Hutchinson, N. Fleck, M. Ashby, H. Wadley, The topological design of multifunctional cellular metals, Prog. Mater. Sci. 46 (34) (2001) 309—327.

[19] B. Wang, G. Cheng, Design of cellular structures for optimum efficiency of heat dissipation, Struct. Multidisc. Optim. 30 (2005) 447—458.

[20] L. Cheng, P. Zhang, J. Toman, Y. Yu, E. Biyikli, M. Kirca, M. Chmielus, A. To, Efficient design-optimization of variable-density hexagonal cellular structure by additive manufacturing: theory and validation, J. Manuf. Sci. Eng. 137 (2015) 021004—021012.

[21] A. Aremu, I. Maskery, C. Tuck, I. Ashcroft, R. Wildman, R. Hague, A comparative finite element study of cubic unit cells for selective laser melting, in: Solid Freeform Symposium, 2014.

[22] D.-J. Yoo, Advanced porous scaffold design using multi-void triply periodic minimal surface models with high surface area to volume ratios, Int. J. Precis.

[23] A. Aremu, J. Brennan-Craddock, A. Panesar, I. Ashcroft, R. Hague, R. Wildman, C. Tuck, A voxel-based method of constructing and skinning conformal and functionally graded lattice structures suitable for additive manufacturing, Addit. Manuf. 13 (2017) 1—13.

[24] C.R. Bowen, I. Turner, R. Gabbrielli, Development of modelling methods for materials to be used as bone substitutes, Key Eng. Mat. 361 (2008) 903—906.

[25] D.-J. Yoo, Heterogeneous porous scaffold design for tissue engineering using triply periodic minimal surfaces, Int. J. Precis. Eng. Mat. 13 (4) (2012) 527—537.

[26] D.-J. Yoo, K.-H. Kim, An advanced multi-morphology porous scaffold design method using volumetric distance field and beta growth function, Int. J. Precis. Eng. Mat. 16 (9) (2015) 2021—2032.

[27] M. Afshar, A.P. Anaraki, H. Montazerian, J. Kadkhodapour, Additive manufacturing and mechanical characterization of graded porosity scaffolds designed based on triply periodic minimal surface architectures, J. Mech. Behav. Biomed. Mater. 62 (2016) 481—494.

[28] D.W. Abueidda, R.K.A. Al-Rub, A.S. Dalaq, D.-W. Lee, K.A. Khan, I. Jasiuk, Effective conductivities and elastic moduli of novel foams with triply periodic minimal surfaces, Mech. Mater. 95 (2016) 102—115.

[29] E.J.W. Crossland, M. Kamperman, M. Nedelcu, C. Ducati, U. Wiesner, D.M. Smilgies, G.E.S. Toombes, M.A. Hillmyer, S. Ludwigs, U. Steiner, H.J. Snaith, A bicontinuous double gyroid hybrid solar cell, Nano Lett. 9 (8) (2009) 2807—2812.

[30] M.R.J. Scherer, L. Li, P.M.S. Cunha, O.A. Scherman, U. Steiner, Enhanced electrochromism in gyroid-structured vanadium pentoxide, Adv. Mater. 24 (9) (2012) 1217—1221.

[31] S.B.G. Blanquer, M. Werner, M. Hannula, S. Sharifi, G.P.R. Lajoinie, D. Eglin, J. Hyttinen, A.A. Poot, D.W. Grijpma, Surface curvature in triply-periodic minimal surface architectures as a distinct design parameter in preparing advanced tissue engineering scaffolds, Biofabrication 9 (2) (2017) 025001.

[32] V. Deshpande, N. Fleck, M. Ashby, Effective properties of the octet-truss lattice material, J. Mech. Phys. Sol. 49 (8) (2001) 1747—1769.

[33] X. Zheng, H. Lee, T.H. Weisgraber, M. Shusteff, J. DeOtte, E.B. Duoss, J.D. Kuntz, M.M. Biener, Q. Ge, J.A. Jackson, S.O. Kucheyev, N.X. Fang, C.M. Spadaccini, Ultralight, ultrastiff mechanical metamaterials, Science 344 (6190) (2014) 1373—1377.

[34] C. Yan, L. Hao, A. Hussein, P. Young, Ti-6Al-4V triply periodic minimal surface structures for bone implants fabricated via selective laser melting, J. Mech. Behav. Biomed. Mater. 51 (2015) 61—73.

[35] C. Yan, L. Hao, A. Hussein, P. Young, J. Huang, W. Zhu, Microstructure and mechanical properties of aluminium alloy cellular lattice structures manufactured by direct metal laser sintering, Mat. Sci. Eng. A Struct. 628 (2015) 238—246.

[36] A.S. Dalaq, D.W. Abueidda, R.K.A. Al-Rub, Mechanical properties of 3D printed interpenetrating phase composites with novel architectured 3D solid-sheet reinforcements, Compos. Part A Appl. S. 84 (2016) 266—280.

[37] A.S. Dalaq, D.W. Abueidda, R.K.A. Al-Rub, I.M. Jasiuk, Finite element prediction of effective elastic properties of interpenetrating phase composites with architectured 3D sheet reinforcements, Int. J. Solids Struct. 83 (2016) 169—182.

[38] K. Ushijima, W. Cantwell, R. Mines, S. Tsopanos, M. Smith, An investigation into the compressive properties of stainless steel micro-lattice structures, J. Sandw. Struct. Mater. 13 (3) (2011) 303—329.

[39] S. Khaderi, V. Deshpande, N. Fleck, The stiffness and strength of the gyroid lattice, Int. J. Solids Struct. 51 (2324) (2014) 3866—3877.

[40] S.C. Kapfer, S.T. Hyde, K. Mecke, C.H. Arns, G.E. Schrder-Turk, Minimal surface scaffold designs for tissue engineering, Biomaterials 32 (29) (2011) 6875—6882.

[41] D. Yoo, New paradigms in internal architecture design and freeform fabrication of tissue engineering porous scaffolds, Med. Eng. Phys. 34 (6) (2012) 762—776.

[42] S. Giannitelli, D. Accoto, M. Trombetta, A. Rainer, Current trends in the design of scaffolds for computer-aided tissue engineering, Acta Biomater. 10 (2) (2014) 580—594.

[43] D. Ngim, J.-S. Liu, R. Soar, Design optimization of consolidated granular-solid polymer prismatic beam using metamorphic development, Int. J. Solids Structs. 46 (3) (2009) 726—740.

[44] M. Ashby, The properties of foams and lattices, Philos. T. Roy. Soc. A 364 (1838) (2006) 15—30.